NASA Technical Memorandum 4712

The C(T) Specimen in Laminated Composites Testing

Levon Minnetyan and Christos C. Chamis

APRIL 1996

National Aeronautics and
Space Administration

NASA Technical Memorandum 4712

The C(T) Specimen in Laminated Composites Testing

Levon Minnetyan
Clarkson University
Potsdam, New York

Christos C. Chamis
Lewis Research Center
Cleveland, Ohio

National Aeronautics and
Space Administration

Office of Management

Scientific and Technical
Information Program

1996

THE C(T) SPECIMEN IN LAMINATED COMPOSITES TESTING

Levon Minnetyan
Clarkson University
Potsdam, New York

and

Christos C. Chamis
National Aeronautics and Space Administration
Lewis Research Center
Cleveland, Ohio

Summary

The use of the compact tension C(T) specimen in laminated composites testing is investigated by considering two examples. A new computational methodology that scales up constituent material properties and stress and strain limits to the structure level is used to evaluate damage propagation stages as well as the structural fracture load. Damage initiation, growth, accumulation, progressive fracture, and ultimate fracture modes are identified. Specific dependences of C(T) specimen test characteristics on laminate configuration and composite constituent properties are quantified.

Introduction

Design considerations with regard to the durability of fiber composite structures require an a priori evaluation of damage initiation and fracture propagation mechanisms under expected loading and service environments. Concerns for safety and survivability of critical components require a quantification of the structural fracture resistance under loading.

Inherent flexibilities in the selection of constituent materials and the laminate configuration make composites more capable of fulfilling structural design requirements. However, those same design flexibilities render the assessment of composite structural response and durability more elaborate, prolonging the design process. It is difficult to design and certify a composite structure because of the complexities in predicting the overall congruity and performance of fibrous composites under various loading and hygrothermal conditions.

Laminated composite design practice has been based on extensive testing with attempts to apply formal fracture mechanics concepts to interpret test results. In certain cases, interpretation of laminated composite test data via fracture mechanics has been satisfactory. However, in most cases, fracture mechanics methods have significantly underpredicted the strength of fiber composites. The reconciliation of test results with fracture mechanics has required significant modifications of effective fracture toughness and specific laminate configuration-dependent effective stress concentration field parameters. Additionally, required adjustments of fracture mechanics parameters have had to be reassessed with every change in constituent and laminate characteristics.

The proposed standard E24.07.02 on the translaminar fracture of composites includes compact tension C(T) specimen testing to generate experimental data with regard to crack propagation, similar to the E399 standard for metals. However, even when C(T) test data were available for a given laminate, many questions about the damage progression characteristics could not be easily answered and sensitive material parameters were difficult to identify. The complete evaluation of laminated composite fracture requires an assessment of ply and supply level damage and/or fracture processes.

The present approach bypasses traditional fracture mechanics to provide an alternative evaluation method, conveying to the design engineer a detailed description of damage initiation, growth, accumulation, and propagation that would take place in the process of the ultimate fracture of a fiber composite structure. Results show in detail the damage progression sequence and structural fracture resistance during different degradation stages. This report demonstrates that computational simulation, with the use of established material modeling and finite element modules, adequately tracks the damage growth and subsequent propagation to fracture of fiber composite specimens.

For the purpose of the present study, the following terminology is used to describe the various stages of degradation in the composite structure: (1) damage initiation refers to the start of damage induced by loading that the composite structure is designed to carry; (2) damage growth is the progression of damage from the location of damage initiation to other regions; (3) damage accumulation is the increase in the amount of damage in the damaged regions with additional damage modes becoming active; (4) damage propagation is the rapid progression of damage to other regions of the structure; (5) structural fracture is the ultimate disintegration of the specimen.

Methodology

The behavior of fiber composite structures under loading is rather complex, especially when possible material degradation resulting from preexisting damage and damage propagation eventually leading to structural fracture is to be considered. Because of the numerous possibilities with combinations of fiber and matrix, laminate configuration, and loading conditions, it is essential to have an integrated and effective computational capability to predict the behavior of composite structures for any loading, geometry, composite material combination, and boundary condition. The predictions of damage initiation, growth, accumulation, and propagation to fracture are important in evaluating the load carrying capacity and reliability of composite structures. The CODSTRAN (COmposite Durability STRuctural ANalysis) computer code (ref. 1) was developed for this purpose. CODSTRAN is able to simulate damage initiation, damage growth, and fracture in composites under various loading and environmental conditions. The simulation of progressive fracture by CODSTRAN has been verified to be in reasonable agreement with experimental data from tensile coupon tests on graphite/epoxy laminates (ref. 2). Recent additions to CODSTRAN have enabled the investigation of the effects of composite degradation on structural response (ref. 3), composite damage induced by dynamic loading (ref. 4), composite structures global fracture toughness (ref. 5), the effect of hygrothermal environment on durability (ref. 6), damage progression in composite shells subjected to internal pressure (ref. 7), an overall evaluation of progressive fracture in polymer matrix composite structures (ref. 8), the durability of stiffened composite shell panels under combined loading (ref. 9), and damage progression in composite shell structures for expeditious and efficient structural design (ref. 10). The purpose of this report is to describe the application of CODSTRAN to simulate progressive fracture in fiber composite compact tension specimens, taking into account damage initiation and/or propagation mechanisms.

CODSTRAN is an integrated, open-ended, stand-alone computer code consisting of three modules: composite mechanics, finite element analysis, and damage progression modeling. The overall evaluation of composite structural durability is carried out in the damage progression module (ref. 1) that monitors composite degradation for the entire structure. The damage progression module relies on ICAN (Integrated Composite Analyzer, ref. 11) for composite micromechanics, macromechanics, and laminate analysis and calls a finite element analysis module that uses anisotropic thick shell elements to model laminated composites (ref. 12).

Figure 1 is a schematic of the computational simulation cycle in CODSTRAN. The ICAN composite mechanics module is called before and after each finite element analysis. Prior to each finite element analysis, the ICAN module computes the composite properties from the fiber and matrix constituent

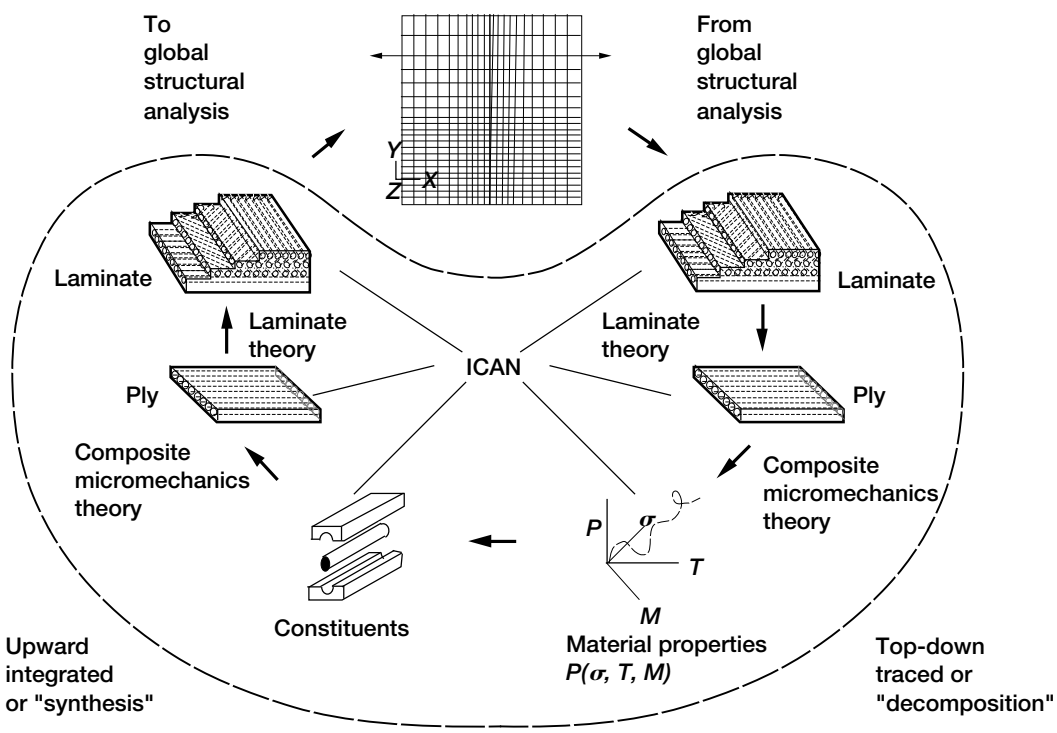

Figure 1.—CODSTRAN (Composite Durability Structural Analysis) progressive fracture simulation cycle.

characteristics and the composite layup. The finite element analysis module accepts the composite properties that are computed by the ICAN module at each node and performs the analysis at each load increment. After an incremental finite element analysis, the computed generalized nodal force resultants and deformations are supplied to the ICAN module that evaluates the nature and amount of local damage, if any, in the plies of the composite laminate. Individual ply failure modes are assessed by ICAN using failure criteria associated with the negative and positive limits of the six ply stress components in the material directions

$$S_{\ell 11C} < \sigma_{\ell 11} < S_{\ell 11T} \tag{1}$$

$$S_{\ell 22C} < \sigma_{\ell 22} < S_{\ell 22T} \tag{2}$$

$$S_{\ell 33C} < \sigma_{\ell 33} < S_{\ell 33T} \tag{3}$$

$$S_{\ell 12(-)} < \sigma_{\ell 12} < S_{\ell 12(+)} \tag{4}$$

$$S_{\ell 23(-)} < \sigma_{\ell 23} < S_{\ell 23(+)} \tag{5}$$

$$S_{\ell 13(-)} < \sigma_{\ell 13} < S_{\ell 13(+)} \tag{6}$$

where $S_{\ell ij\alpha}$ represents the ply stress limit in which the ij subscript indicates the stress component and the α subscript indicates the sense as tension and/or compression for normal stresses and as $\pm$ for shear stress limits on the ply; σ is the ply stress. The ICAN composite mechanics module computes $S_{\ell ij\alpha}$ stress limits.

In addition to the failure criteria F based on the above stress limits, a modified distortion energy (MDE) failure criterion that takes into account combined stresses is considered (ref. 11). The MDE failure criterion is expressed as

$$F = 1 - \left[\left(\frac{\sigma_{\ell 11\alpha}}{S_{\ell 11\alpha}} \right)^2 + \left(\frac{\sigma_{\ell 22\beta}}{S_{\ell 22\beta}} \right)^2 - K_{\ell 12} \frac{\sigma_{\ell 11\alpha}}{S_{\ell 11\alpha}} \frac{\sigma_{\ell 22}}{S_{\ell 22}} + \left(\frac{\sigma_{\ell 12S}}{S_{\ell 12S}} \right)^2 \right] \tag{7}$$

where α and β indicate tensile or compressive stress, $S_{\ell 11\alpha}$ is the ply longitudinal strength in tension or compression, $S_{\ell 22\alpha}$ is the transverse strength in tension or compression, and

$$K_{\ell 12} = \frac{\left(1 + 4\nu_{\ell 12} - \nu_{\ell 13}\right)E_{\ell 22} + \left(1 - \nu_{\ell 23}\right)E_{\ell 11}}{\left[E_{\ell 11}E_{\ell 22}\left(2 + \nu_{\ell 12} + \nu_{\ell 13}\right)\left(2 + \nu_{\ell 21} + \nu_{\ell 23}\right)\right]^{1/2}} \tag{8}$$

The type of failure is assessed by comparing the magnitudes of the squared terms in equation (7). Depending on the dominant term in the MDE failure criterion, fiber failure or matrix failure is assigned. If the first squared term in equation (7) that corresponds to ply longitudinal tensile or compressive failure is dominant, fiber failure is assigned. On the other hand, if one of the other squared terms correponding to ply transverse tensile or compressive failure or to ply shear failure is dominant, matrix failure is assigned.

Interply delamination due to the relative rotation of the plies is assessed by evaluating the rotation between adjacent plies $\Delta\phi$ from the composite deformations and ply fiber angles (ref. 11):

$$\Delta\phi = \frac{1}{2}\left(\varepsilon_{cyy} - \varepsilon_{cxx}\right)\left(\sin 2\theta_i - \sin 2\theta_{i-1}\right) + \frac{1}{2}\varepsilon_{cxy}\left(\cos 2\theta_i - \cos 2\theta_{i-1}\right)\left(\varepsilon_{cx}\right) \tag{9}$$

where ε is the composite strain with respect to the structural axis and θ_i represents the fiber orientation of the ith ply. The delamination criterion is given by

$$D = \left(1 - \frac{|\Delta\phi|}{\Delta\phi_{del}}\right) \tag{10}$$

If D is negative delamination, failure due to ply relative rotation is predicted.

The generalized stress-strain relationships are revised locally according to the composite damage evaluated after each finite element analysis. The model is automatically updated with a new finite element mesh having reconstituted composite structural properties, and the structure is reanalyzed for further deformation and damage. If there is no damage after a load increment, the structure is considered to be in equilibrium and an additional load increment is applied, leading to possible damage growth, accumulation, or propagation. Simulation is continued until global fracture when the specimen is broken into two pieces.

Graphite/Epoxy Specimen

The structural example for this case was a C(T) specimen consisting of AS-4 graphite fibers in a low-modulus, high-strength (LMHS) toughened epoxy matrix. The fiber and matrix properties were obtained from a data bank (ref. 11) of composite constituent material properties resident in CODSTRAN. The corresponding fiber and matrix properties are given in the appendix. The LMHS matrix properties were representative of the 977-2 resin. The fiber volume ratio was 60 percent. The laminate structure consisted of thirty-six 0.133-mm (0.00525-in.) plies, resulting in a composite

thickness of 4.80 mm (0.189 in.). The laminate configuration was $[0_2/90]_{6s}$. The 0° plies were in the direction of loading and the 90° plies were perpendicular to the load direction. The C(T) specimen (fig. 2) had a height $2H$ of 30 mm (1.18 in.), an effective width W (distance between load line and backface) of 25.0 mm (0.984 in.), a notch slot height $2h$ of 0.3 mm (0.012 in.), and a distance between load line and notch tip a of 12.5 mm (0.492 in.). A computational model of the specimen was prepared using 420 rectangular thick shell elements with 467 nodes (shown in fig. 3). Pin holes were not modeled in the finite element representation of the specimen to enable nodal support and loading. The finite element model was configured to have a nodal point at the center of each pin hole. One of the load points was restrained in all degrees of freedom except for θ_z. The other load point was restrained only in the displacement u_y-, u_z-, θ_x-, and θ_y-directions but was allowed freedom in the u_x-, and θ_z-directions. These boundary conditions are representative of inserting a stationary reaction pin into one of the pin holes and inserting a movable loading pin in the other pin hole. A concentrated tensile load was applied in the u_x direction. The load was increased gradually.

Figure 4 shows N_x generalized stress resultant contours under a 1779-N (400-lb) load prior to damage initiation. The maximum tensile stresses were concentrated at the tip of the preexisting notch. There was a distinct compression zone at the backface of the specimen opposite the notch.

Figure 5 shows N_y generalized stress contours under the 1779-N (400-lb) load. The maximum tensile stresses were concentrated at the tip of the preexisting notch. There were distinct compression zones at the two sides of the specimen opposite the notch tip.

Figure 6 shows N_{xy} generalized shear stress contours under the 1779-N (400-lb) load. The maximum shear stresses were concentrated halfway between the notch tip and back corners of the specimen.

The generalized stress contours shown in figures 4 to 6 indicate possible locations of damage initiation and progression. Computational simulation showed damage initiation at 2091 N (470 lb) by matrix cracking due to transverse tensile failures in the 90° plies at the notch tip. Damage growth continued gradually at the vicinity of the notch tip by matrix cracking of both the 90° as well as the 0° plies until a load of 3114 N (700 lb) was reached. Above 3114 N (700 lb), new damage zones were formed as a result of compressive failures of the 0° plies at the backface and matrix shear failures halfway between the notch tip and corners of the specimen. At 3745 N (842 lb) additional damage zones were formed as a result of new compressive failures of the 0° plies at the backface, compressive failure of the 90° plies at the sides, and the growth of matrix shear failures halfway between the notch tip and corners of the specimen. Because there were no fiber failures at the notch tip, it remained at its original position . When loading was increased to 3767 N (847 lb), damage increased significantly with through-the-thickness fracture of the compression and shear failure zones, but the increase was without notch extension. The simulated ultimate load was reached at 3870 N (870 lb) because of the coalescence of shear and compressive damage zones in the notch tip and disintegration of the specimen.

Figure 7 shows the physical locations of the damage progression modes given in numerical sequence from 1 (indicating the damage initiation zone) to 4 (indicating the last location of damage growth that occurred at the ultimate load). The distinct characteristics of the four damage modes may be summarized as follows: (1) damage initiation at the crack tip by matrix cracking due to ply transverse tensile $\sigma_{\ell 22T}$ failures that

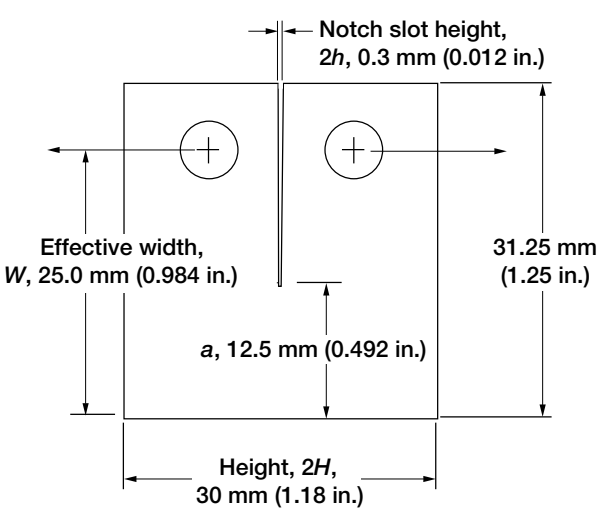

Figure 2.—Graphite/epoxy $[0_2/90]_{6s}$ compact tension C/(T) specimen.

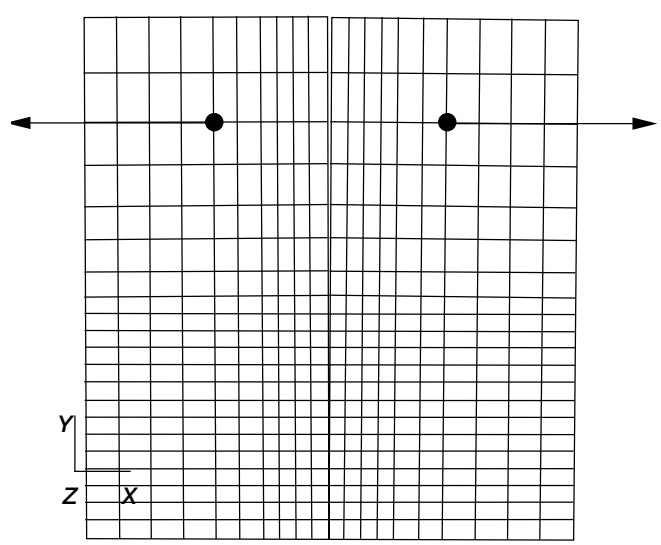

Figure 3.—Graphite/epoxy $[0_2/90]_{6s}$ C(T) specimen finite element model (467 nodes, 420 quadrilateral elements).

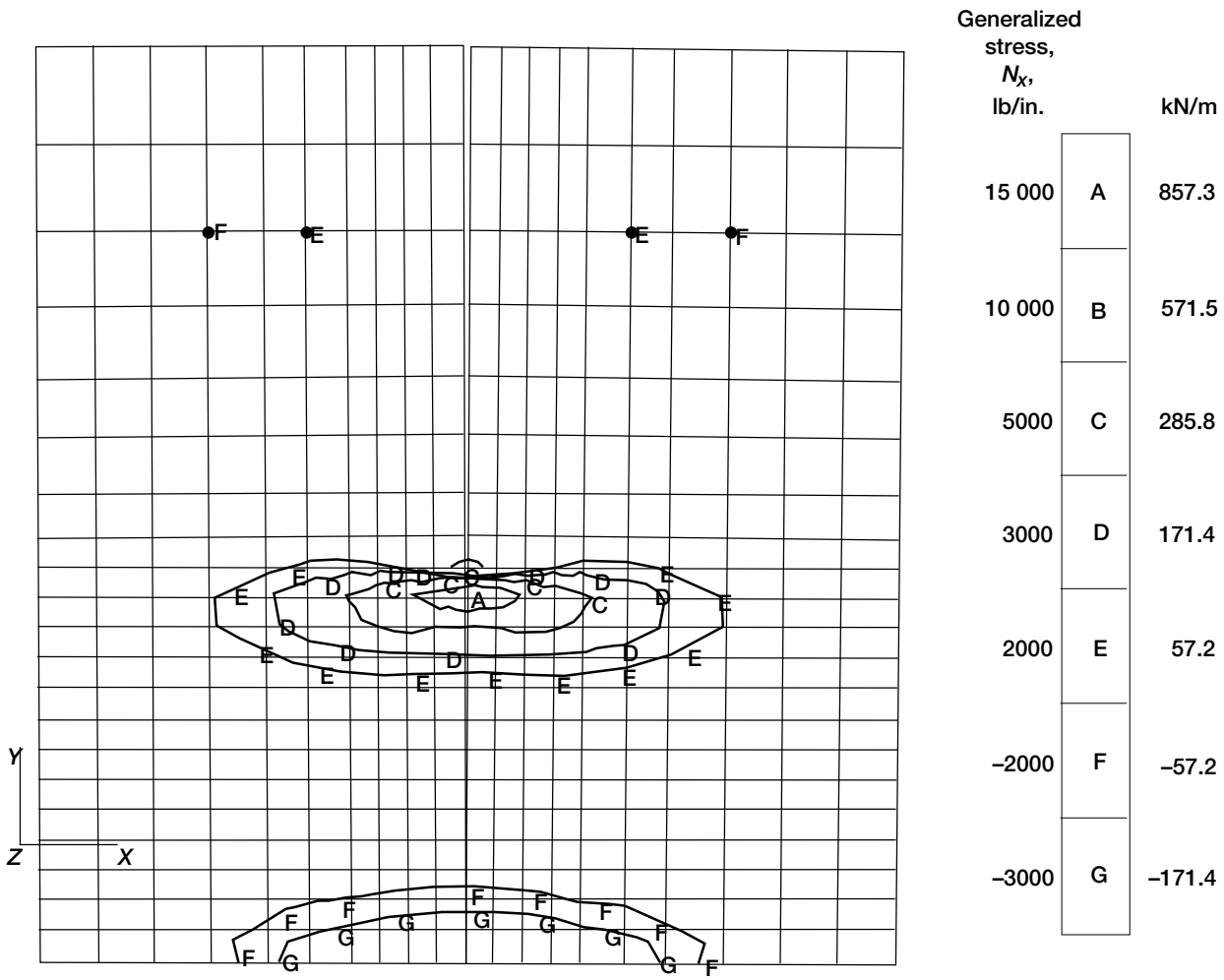

Figure 4.—General stresses N_x under 1779–N (400–lb) load for graphite/epoxy $[0_2/90]_{6s}$ C(T) specimen.

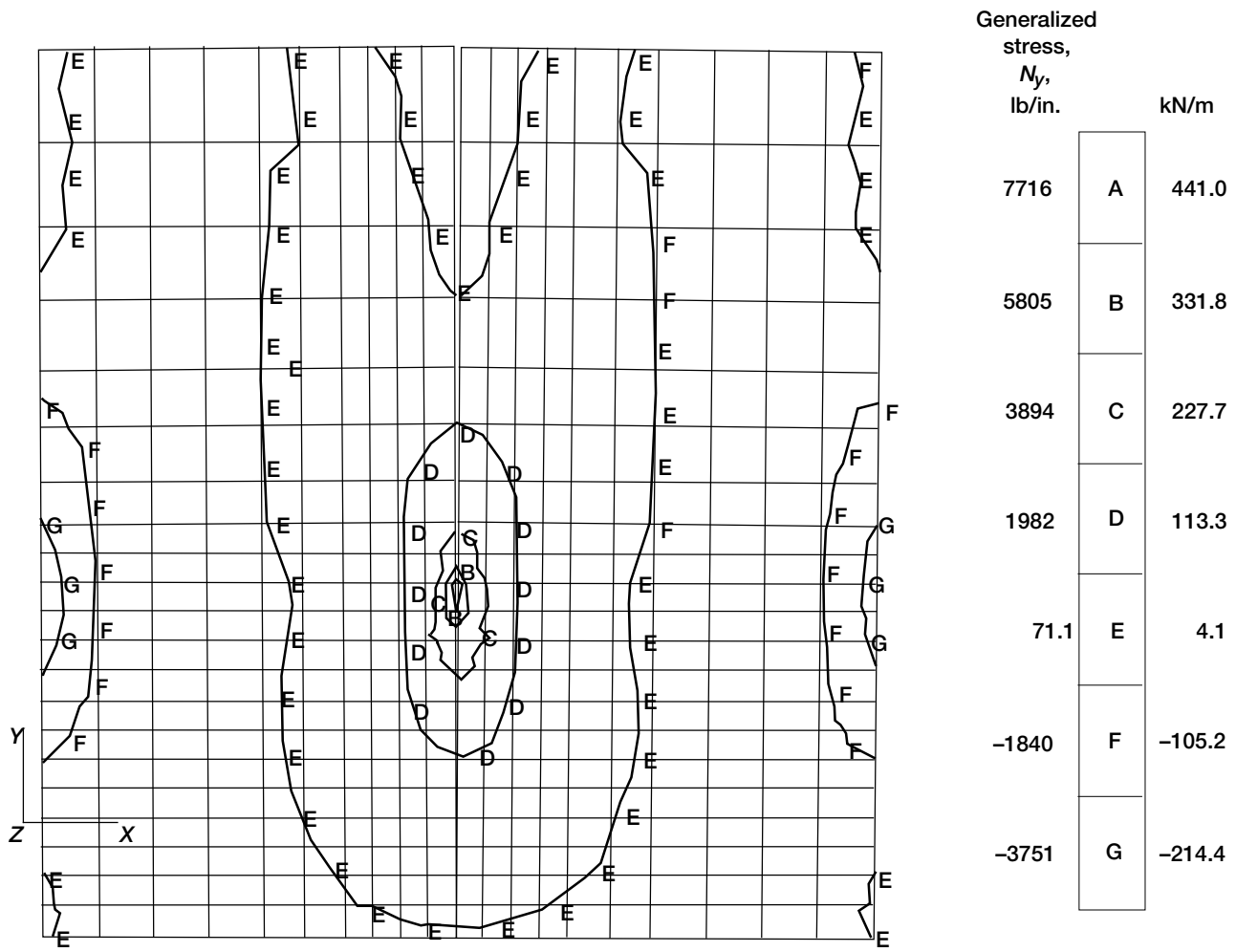

Figure 5.—General stresses N_y under 1779–N (400–lb) load for graphite/epoxy $[0_2/90]_{6s}$ C(T) specimen.

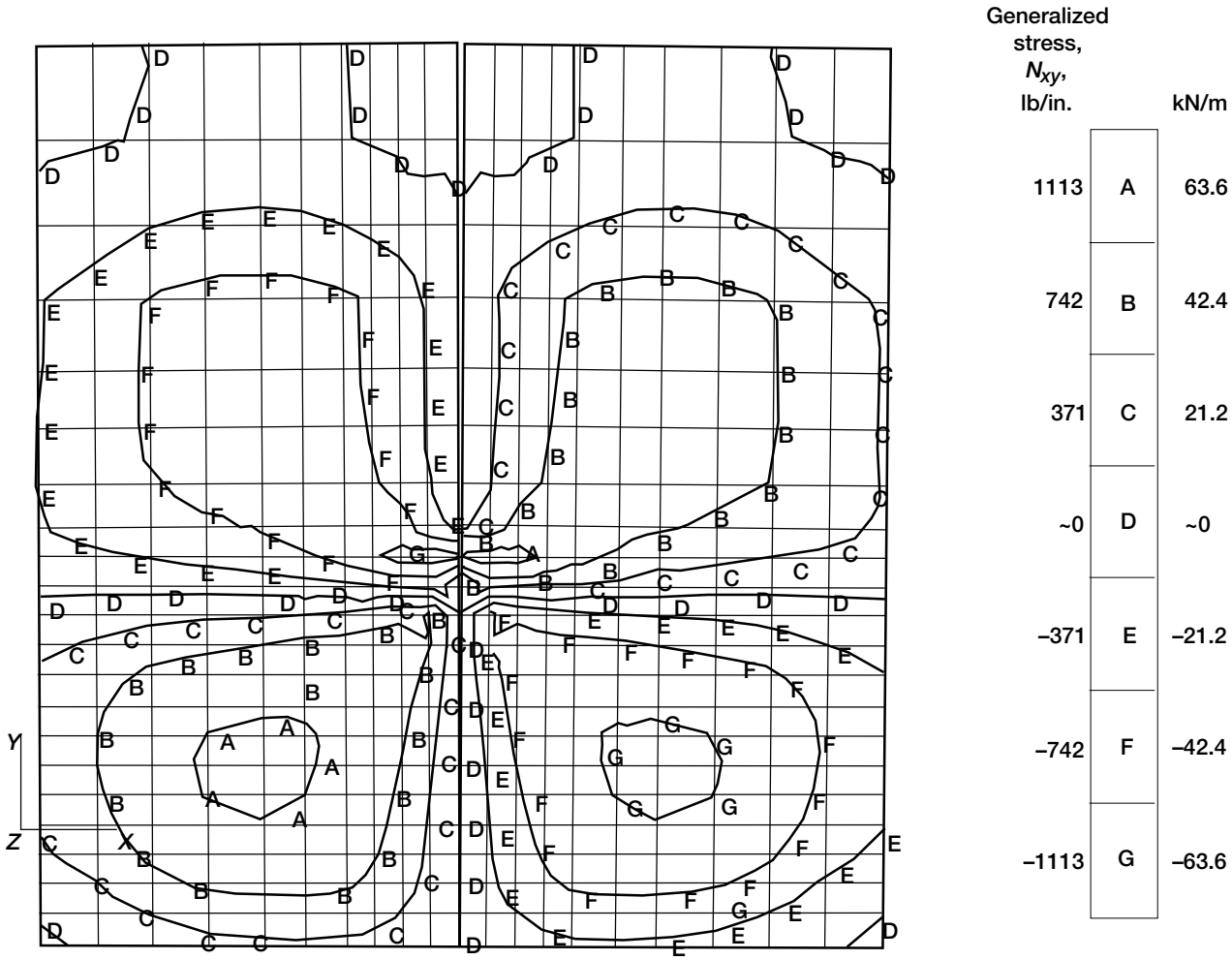

Figure 6.—General stresses N_{xy} under 1779–N (400–lb) load for graphite/epoxy $[0_2/90]_{6s}$ C(T) specimen.

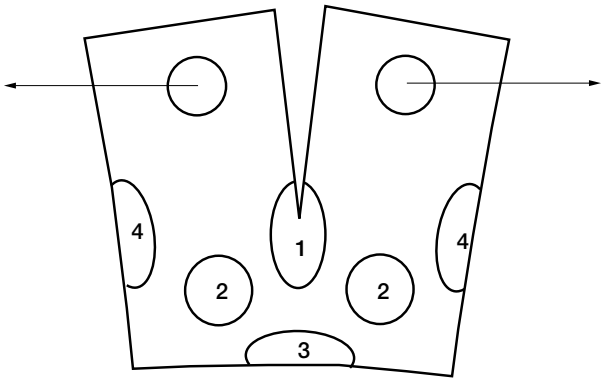

Figure 7.—Damage progression sequence and locations for graphite/epoxy $[0_2/90]_{6s}$ C/(T) specimen. (1) Matrix cracking at notch tip; (2) Shear failure zones; (3) Compression failure at backface; (4) Compression failures at sides.

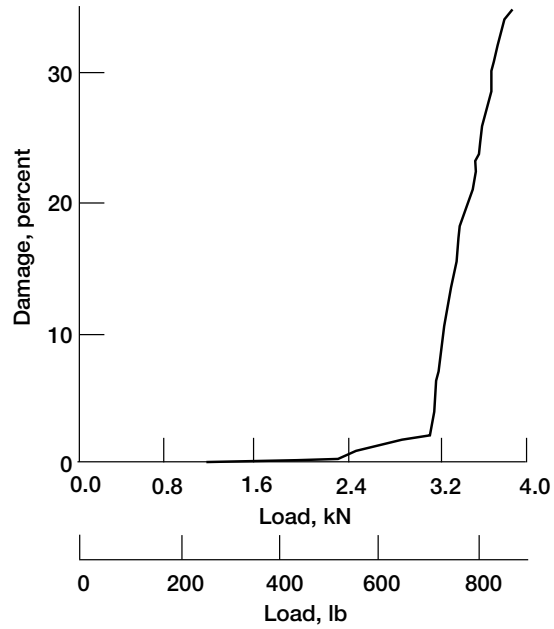

Figure 8.—Damage progression with loading for graphite/epoxy $[0_2/90]_{6s}$ C(T) specimen.

occur in the 90° and the 0° plies, (2) matrix cracking due to $\sigma_{\ell 12S}$ in-plane shear failures in the 90° and 0° plies, (3) fiber fractures due to $\sigma_{\ell 11C}$ longitudinal compression failures in the 0° plies at the backface, and (4) fiber fractures due to $\sigma_{\ell 11C}$ longitudinal compression failures in the 90° plies at the sides of the specimen.

Figure 8 shows the damage progression with applied loading indicating that the rate of damage propagation is increased considerably after the 3114-N (700-lb) loading is exceeded. The scalar damage variable shown in figure 8 is derived from the total volume of the composite material affected by the various damage mechanisms. The percent damage shown on the ordinate of figure 8 is computed by dividing the damaged volume by the total volume of the specimen and multiplying by 100.

The global damage energy release rate (DERR) is defined as the rate of work done by external forces during structural degradation with respect to the damage produced (ref. 5). The DERR can be used to evaluate structural resistance against damage propagation at different stages of loading. Figure 9 shows the DERR as a function of loading indicating significant DERR levels at damage initiation, at the beginning of the damage propagation phase, and at the ultimate load. Figure 10 shows load versus the crack opening displacement (COD) and indicates that the damage initiation and growth stages are not discernable from the load-COD relationship for this case. Nonlinear behavior is only apparent as the ultimate load is approached.

A displacement-controlled laboratory test reached 3959 N (890 lb) at the peak load for this specimen and the overall test response was consistent with computational simulations. However, the damage initiation and growth stages were not discernable from test data. Computational simulation was able to fill in the degradation details that were needed to completely assess fracture characteristics. Computer simulation also indicated that the ultimate load was sensitive to the matrix shear strength for this specimen.

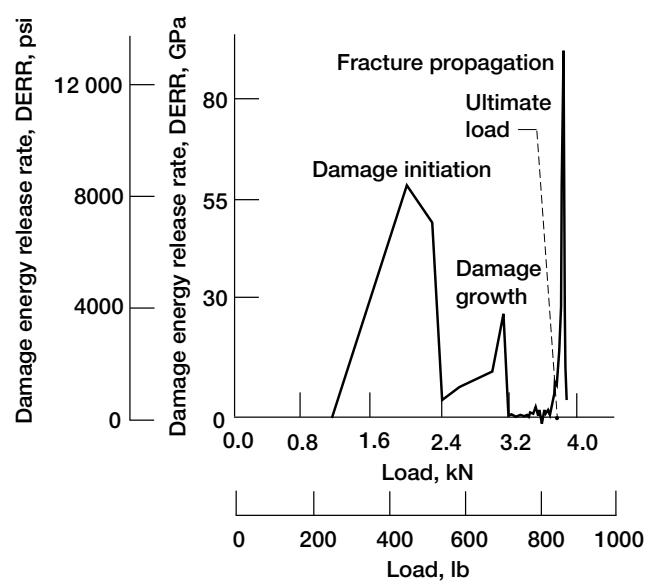

Figure 9.—Damage energy release rate with loading for graphite/epoxy $[0_2/90]_{6s}$ C(T) specimen.

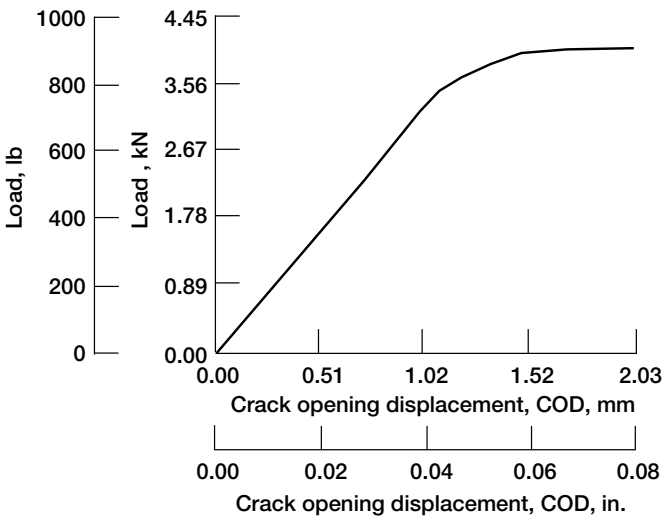

Figure 10.—Load-displacement relationship for graphite/epoxy $[0_2/90]_{6s}$ C(T) specimen.

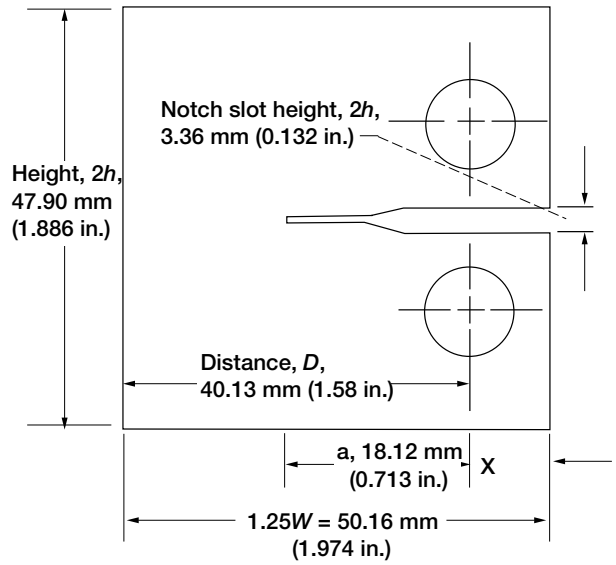

Figure 11.—Ceramic matrix composite C(T) specimen.

Ceramic Matrix Composite Specimen

Progressive fracture of a ceramic matrix fiber composite C(T) specimen was computationally simulated. The composite system consisted of SiC (Nicalon) fibers in a glass (1723) matrix. The fiber volume ratio was 45 percent. The laminate structure consisted of twelve 0.213-mm (0.00837-in.) plies, resulting in a composite thickness of 2.55 mm (0.100 in.). Each of the twelve plies was 0.2125 mm (0.00837 in.) thick. The laminate configuration was $[0/90]_{3s}$. The C(T) specimen (fig. 11) had a half-height H of 23.95 mm (0.943 in.), a width (distance between load line and backface) D of 40.13 mm (1.58 in.), a half-height of notch slot h of 1.68 mm (0.066 in.), and a distance between load line and notch tip a of 18.12 mm (0.713 in.). The specimen complied with ASTM E399 specifications.

As shown in figure 12, the finite element model contained 161 nodes and 130 quadrilateral thick shell elements; the 0° plies were oriented along the x-axis and the 90° plies along the y-axis. As in the previous example, pin holes were not modeled in the finite element representation of the specimen to enable nodal support and loading. The finite element model was configured to have a nodal point at the center of each pin hole. One of the load points was restrained in all degrees of freedom except for θ_z. The other load point was restrained only in the u_y-, u_z-, θ_x-, θ_y-directions but was allowed free movement in the u_x, and θ_z directions. A concentrated tensile load was applied in the u_x-direction. The load was increased gradually. In this case progressive fracture of the C(T) specimen became strongly characterized by longitudinal tensile failures of the 0° plies at the notch tip. Figure 13 shows ply 1 (0° ply) longitudinal stress contours under a 445-N (100-lb) loading prior to damage initiation. The maximum tensile stresses were concentrated at the tip of the preexisting notch. There was a distinct compression zone at the backface of the specimen opposite the notch.

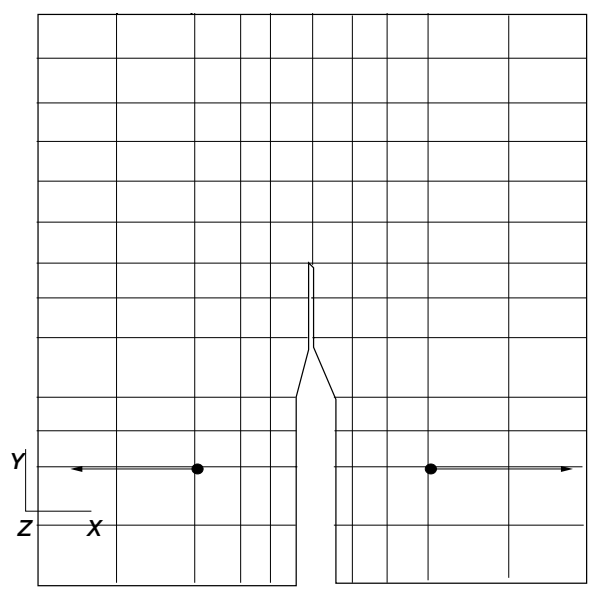

Figure 12.—Ceramic matrix composite C(T) specimen finite element model for silicon carbide (SiC)/glass $[0/90]_{3s}$ (161 nodes, 130 quadrilateral elements).

The CODSTRAN simulation of the SiC/glass C(T) specimen indicated a damage initiation load of 667 N (150 lb). Initial damage was in the form of fiber fracture by longitudinal failure of the 0° plies at the notch tip. When the load was further

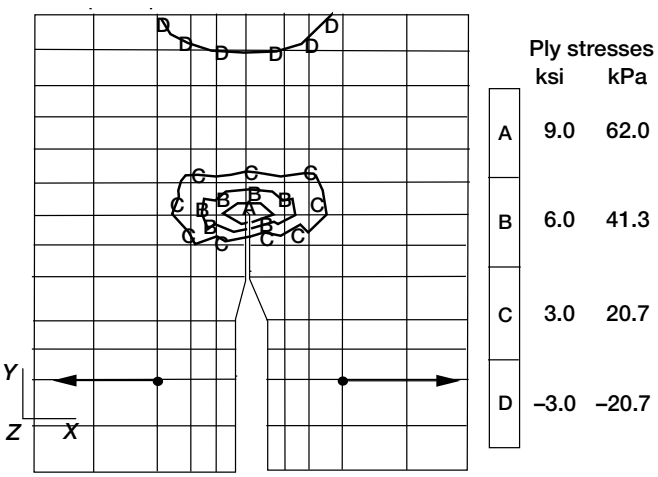

Figure 13.—Ply 1 longitudinal stresses under 445-N (100-lb) load in SiC/glass $[0/90]_{3S}$ C(T) specimen.

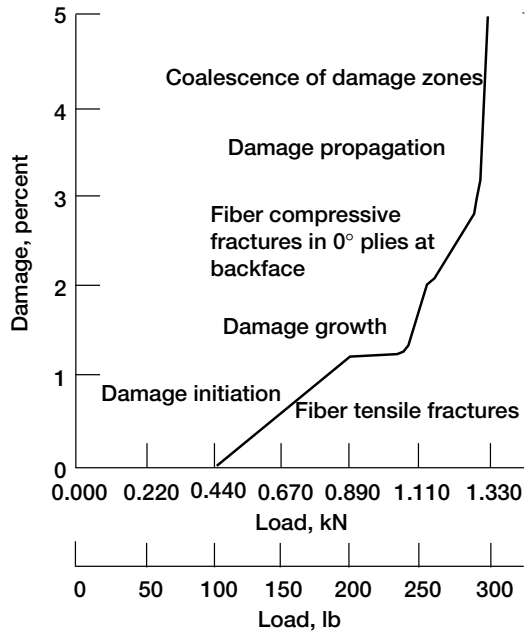

Figure 14.—Damage propagation with loading for SiC glass $[0/90]_{3S}$ C(T) specimen.

increased, fiber fractures and matrix cracking due to excessive transverse ply stresses spread to all plies at the notch tip and immediately ahead of it. Computational simulation took into account nonlinearities due to material and structural effects and showed the details of progressive damage and fracture propagation in the composite structure up to the global fracture of the specimen. Global fracture occurred at 1320 N (297 lb), breaking the specimen into two pieces.

A comparison of the damage progression characterictics of the SiC/glass $[0/90]_{3S}$ C(T) specimen with those of the graphite/epoxy $[0_2/90]_{6S}$ C(T) specimen indicates that the response of the SiC/glass specimen was governed by the fiber properties whereas the response of the graphite/epoxy specimen was controlled by matrix properties. The laminate configuration and the relative moduli and strength of the fiber and matrix constituents play important roles in determining what parameters will be sensitive for the notch toughness of a composite laminate. The in situ constituent properties used in the computational simulation of the SiC/glass C(T) specimen progressive fracture are given in the appendix.

Figure 14 shows the relationship between structural damage and the applied loading for the SiC/glass C(T) specimen. The damage initiation stage corresponds to the development of a damage zone at the notch tip by longitudinal tensile fractures of the 0° plies. Fiber fractures in the 0° plies were followed by the fracture of the 90° plies. The damage initiation stage was concluded at a 0.890-kN (200-lb) load by the formation of a damage/fracture zone at the tip of the original notch. After the damage initiation stage, the loading was increased to 1.045 kN (235 lb) without additional damage. When the load was increased beyond 1.045 kN, damage growth occurred by compressive fractures of the 0° plies at the backface of the specimen opposite the notch. Compressive failure at the backface of the specimen in turn caused tensile failures at the damage zone at the notch tip. The process of alternating compressive and tensile failures was continued until the final damage propagation stage was reached when compressive and tensile fracture zones coalesced and the C(T) specimen was broken into two pieces.

Figure 15 shows the progression of fracture alternately from the tensile zone at the notch tip and from the compressive zone at the backface of the SiC/glass specimen. Figure 16 shows the DERR as a function of the applied tensile loading on the ceramic matrix fiber composite C(T) specimen. The DERR for damage initiation was relatively small, indicating low resistance to damage initiation under tensile loading. However, after the damage initiation stage, the DERR reached considerably higher levels, indicating greater structural resistance to damage propagation prior to global fracture.

When the DERR for the SiC/glass C(T) specimen given in figure 15 is contrasted to the DERR for the graphite/epoxy C(T) specimen given in figure 9, the main difference is observed in the DERR levels at damage initiation. In the case of the graphite/epoxy specimen, the relatively high DERR level at damage initiation, representing a high structural resistance to damage initiation, indicates a well-defined damage initiation load that mainly depends on global structural parameters. Therefore, variations in the local material properties will not have an extraordinary effect on the structural fracture of the graphite/epoxy specimen. On the other hand, for the SiC/glass C(T) specimen, the initial DERR level is very low, indicating a low structural resistance to damage initiation. Accordingly, the damage initiation characteristics of the SiC/Glass C(T) specimen will be extraordinarily sensitive to local SiC fiber strength variations at the notch tip.

1. Damage initiation by fiber fractures at notch tip, 667 N (150 lb)

2. Damage progression by fiber fractures and notch extension, 890 N (200 lb)

3. Compressive failures ($\sigma_{\ell 11C}$) at backface of specimen, 956 to 987 N (215 to 222 lb)

4. Fiber fractures and notch extension, 1053 N (237 lb)

5. Growth of compressive failures at back of specimen, 1053 to 1076 N (237 to 242 lb)

6. More compressive failure growth accompanied by additional fiber fractures at crack tip, 1209 to 1316 N (272 to 296 lb)

7. Global fracture: specimen breaks, 1320 N (297 lb)

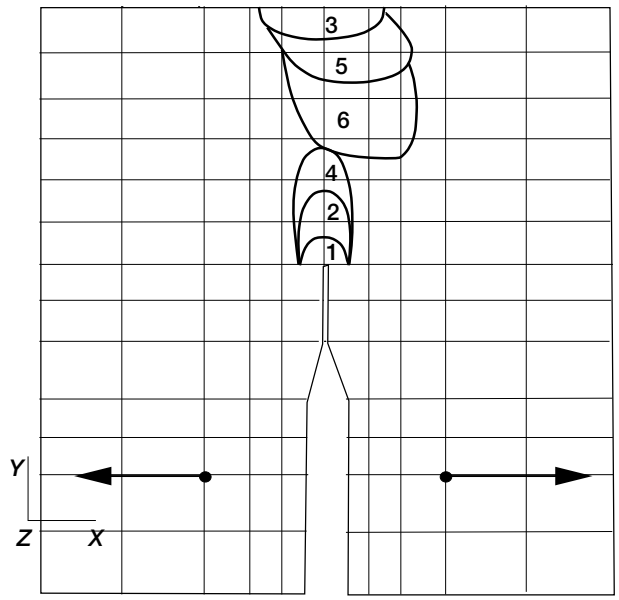

Figure 15.—Damage progression sequence and locations in SiC/glass $[0/90]_{3s}$ C(T) specimen.

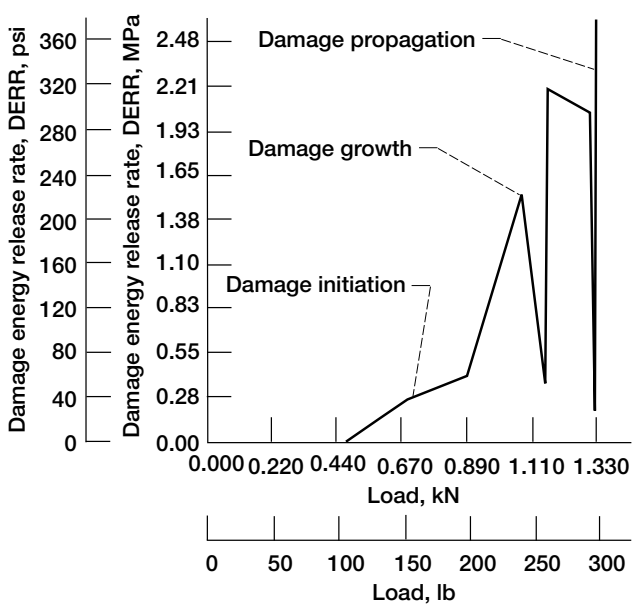

Figure 16.—Damage energy release rates with loading for SiC/glass $[0/90]_{3s}$ C(T) specimen.

Figure 17 shows the load-versus-displacement relationship for the SiC/glass C(T) specimen. The transition from damage initiation to damage growth is not easily discernible from the load-displacement relationship. However, as the damage propagation stage begins, the load-displacement behavior becomes highly nonlinear. At the structural fracture stage, the displacement increases without any increase in the loading.

The global fracture load of 1.320 kN (297 lb) obtained by computational simulation favorably compared with the 1344-N (302-lb) fracture load observed experimentally, as reported in reference 13.

A parametric study via computational simulation indicated that damage initiation and progression are very sensitive to the fiber tensile strength for this specimen. Figure 18 shows the variation in the structural fracture load and the damage initiation load as functions of the fiber tensile strength. In particular, if the fiber strength increases above the 276-MPa (40-ksi) in situ strength of SiC fibers, the fracture load increases at a very steep rate. The main reason for the steep increase in the specimen strength with increased fiber strength is the ability of the stronger fibers to impede damage initiation at the notch tip. This phenomenon explains some of the difficulty in fitting experimental data to a traditional fracture toughness parameter for the room-temperature fracture of similar ceramic matrix C(T) specimens (ref.13).

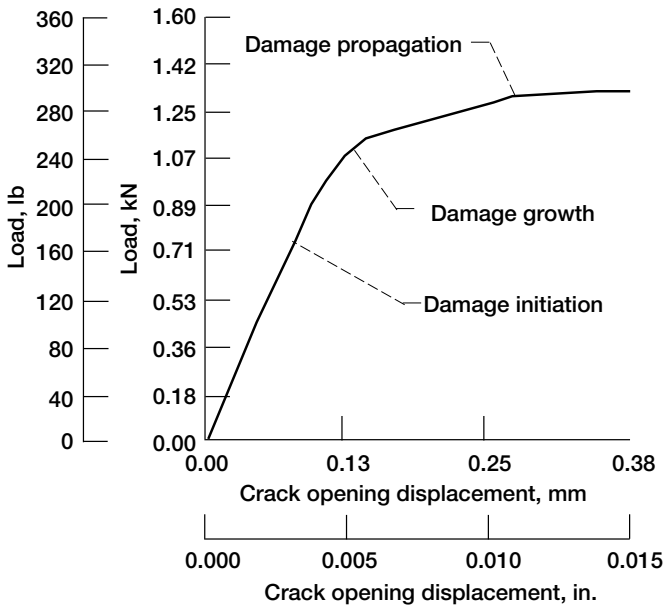

Figure 17.—Load-displacement relationship in SiC/glass $[0/90]_{3s}$ C(T) specimen.

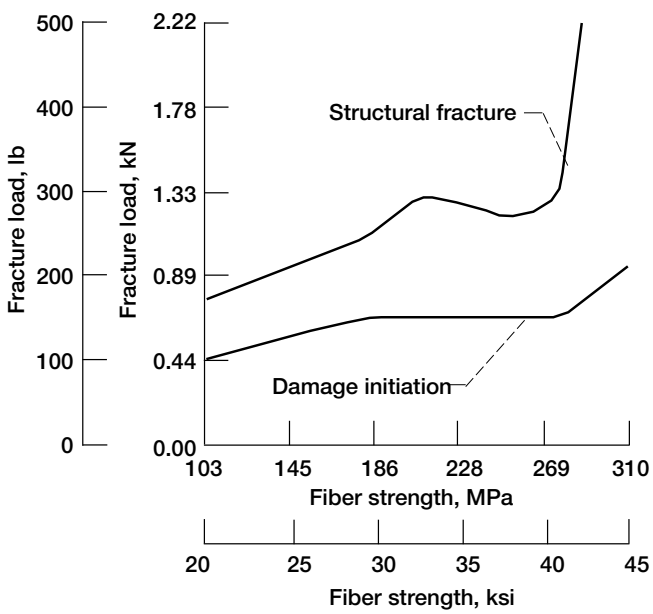

Figure 18.—Effect of fiber strength on fracture in SiC/glass $[0/90]_{3s}$ C(T) specimen.

Summary of Results

Computational simulation was used to evaluate damage growth and propagation to fracture for graphite/epoxy and silicon carbide (SiC)/fiber glass-matrix composite compact tension C(T) specimens. The demonstrated procedure is flexible and applicable to all types of constituent materials, structural geometry, and loading. Hybrid composite structures, composites containing homogeneous materials (e.g., metallic layers), and binary composites can be simulated. The significant results from this investigation are as follows:

1. Computational simulation, with the use of established composite mechanics and finite element modules, can predict the influence of an existing notch, as well as loading, on the safety and durability of fiber composite structures.
2. Computational simulation adequately tracks the damage growth and subsequent propagation to fracture for fiber composite C(T) specimens.
3. Computational simulation can be used prior to testing to identify locations and modes of composite damage that need to be monitored by proper instrumentation and inspection of the specimen during a laboratory experiment.
4. Interpretation of experimental data can be significantly facilitated by the detailed results of a computational simulation.
5. Computational simulation provides detailed information on damage initiation/progression mechanisms and identifies sensitive material parameters affecting structural fracture.
6. Fracture toughness parameters such as the structural fracture load are identifiable for any specimen or structure by the demonstrated method.
7. Computational simulation represents a new global approach that may be used for progressive damage and fracture assessment in design investigations.

Lewis Research Center
National Aeronautics and Space Administration
Cleveland, Ohio , October 18, 1995

Appendix—Fiber and Matrix Properties

AS–4 GRAPHITE FIBER

Number per end	10 000
Diameter, mm (in.)	0.00762 (0.300×10^{-3})
Density, kg/m^3 (lb/in.^{3})	4.04×10^{-7} (0.063)
Normal modulus, GPa (psi)	
Longitudinal	227 (32.90×10^6)
Transverse	13.7 (1.99×10^6)
Poisson's ratio	
ν_{12}	0.20
ν_{23}	0.25
Shear modulus, GPa (psi)	
G_{12}	13.8 (2.00×10^6)
G_{23}	0.90 (1.00×10^6)
Thermal expansion coefficient, / °C (/ °F)	
Longitudinal	1.0×10^{-6} (-0.55×10^{-6})
Transverse	1.0×10^{-6} (-0.56×10^{-6})
Heat conductivity, J-m/hr/m^2/°C (Btu-in./hr/in.^{2}/°F)	
Longitudinal	43.4 (580)
Transverse	4.34 (58)
Heat capacity, J/kg/°C (Btu/lb/°F)	712 (0.17)
Strength, MPa (ksi)	
Tensile	3723 (540)
Compressive	3351 (486)

LOW-MODULUS, HIGH-STRENGTH TOUGHENED EPOXY MATRIX

Density, kg/m^3 (lb/in.^{3})	3.20×10^{-7} (0.0430)
Normal modulus, GPa (kpsi)	2.41 (350)
Poisson's ratio, ν	0.43
Coefficient of thermal expansion, / °C (/ °F)	1.03 (0.57×10^{-4})
Heat conductivity, J-m/hr/m^2/°C (Btu-in./hr/in.^{2}/°F)	930 (1.25)
Heat capacity, J/kg/°C (Btu/lb/°F)	738 (0.25)
Strength, MPa (ksi)	
Tensile	121 (17.5)
Compressive	242 (35.0)
Shear	93.4 (13.5)
Allowable strain	
Tensile	0.08
Compressive	0.15
Shear	0.1
Torsional	0.1
Void conductivity, J-m/hr/m^2/°C (Btu-in./hr/in.^{2}/°F)	16.8 (0.225)
Glass transition temperature, °C (°F)	180 (350)

SILICON CARBIDE (NICALON) FIBER

Fibers per end	1
Diameter, mm (in.)	0.012 (0.472×10^{-3})
Density, kg/m^3 (lb/in.^{3})	2.07×10^{-6} (0.278)
Normal modulus, GPa (psi)	
Longitudinal	200 (29.0×10^6)
Transverse	200 (29.0×10^6)
Poisson's ratio	
ν_{12}	0.30
ν_{23}	0.30
Shear modulus, GPa (psi)	
G_{12}	77.2 (11.2×10^6)
G_{12}	77.2 (11.2×10^6)
Thermal expansion coefficient, / °C (/ °F)	
Longitudinal	4.57×10^{-6} (2.54×10^{-6})
Transverse	4.57×10^{-6} (2.54×10^{-6})
Heat conductivity, J-m/hr/m^2/°C (Btu-in./hr/in.^{2}/°F)	
Longitudinal	8.08 (108)
Transverse	8.08 (108)
Heat capacity, J/kg/°C (Btu/lb/°F)	503 (0.12)
Strength, MPa (ksi)	
Tensile	276 (40)
Compressive	276 (40)

GLASS (1723) MATRIX

Density, kg/m^3 (lb/in.^{3})	6.70×10^{-7} (0.090)
Normal modulus, GPa (ksi)	85.5 (12 400)
Poisson's ratio, ν	0.22
Coefficient of thermal expansion, /°C (/°F)	6.70×10^{-6}(1.21×10^{-5})
Heat conductivity, J-m/hr/m^2/°C (Btu-in./hr/in.^{2}/°F)	5580 (7.5)
Heat capacity, J/kg/°C (Btu/lb/°F)	502 (0.17)
Strength, MPa (ksi)	
Tensile	207 (30.0)
Compressive	2.07 (300)
Shear	207 (30.0)
Allowable strain	
Tensile	0.0073
Compressive	0.0073
Shear	0.0124
Torsional	0.0124
Void conductivity, J-m/hr/m^2/°C (Btu-in./hr/in.^{2}/°F)	16.8 (0.225)
Glass transition temperature, °C (°F)	816 (1500)

References

1. Chamis, C.C.; and Smith, G.T.: CODSTRAN: Composite Durability Structural Analysis. NASA TM–79070, 1978.
2. Irvine, T.B.; and Ginty, C.A.: Progressive Fracture of Fiber Composites. J. Compos. Mater. vol. 20, March 1986, pp. 166–184.
3. Minnetyan, L.; Chamis, C.C.; and Murthy, P.L.N.: Structural Behavior of Composites With Progressive Fracture. J. Reinf. Plast. Comp., vol. 11, no. 4, Apr. 1992, pp. 413–442.
4. Minnetyan, L.; Chamis, C.C.; and Murthy, P.L.N.: Progression of Damage and Fracture in Composites Under Dynamic Loading. NASA TM–103118, 1990.
5. Minnetyan, L.; Murthy, P.L.N.; and Chamis, C.C.: Composite Structure Global Fracture Toughness via Computational Simulation. Comput. Struct., vol. 37, no. 2, 1990, pp. 175–180.
6. Minnetyan, L.; Murthy, P.L.N.; and Chamis, C.C.: Progressive Fracture in Composites Subjected to Hygrothermal Environment. AIAA Paper 91–1140 (NASA TM–105230), 1991.
7. Minnetyan, L.; Chamis, C.C.; and Murthy, P.L.N.: Damage and Fracture in Composite Thin Shells. NASA TM–105289, 1991.
8. Chamis, C.C.; Murthy, P.L.N.; and Minnetyan, L.: Progressive Fracture of Polymer Matrix Composite Structures: A New Approach. NASA TM–105574, 1992.
9. Minnetyan, L., et al.: Structural Durability of Stiffened Composite Shells. Proceedings of the 33rd Structures, Structural Dynamics and Materials Conference, AIAA Paper 92–2244 (NASA CR–190588), vol. 5, 1992, pp. 2879–2886.
10. Minnetyan, L.; and Murthy, P.L.N.: Design for Progressive Fracture in Composite Shell Structures. Proceedings of the 24th International SAMPE Technical Conference, SAMPE, Covina, CA, 1992, pp. T227–T240.
11. Murthy, P.L.N.; and Chamis, C.C.: Integrated Composite Analyzer (ICAN): Users and Programmers Manual. NASA TP–2515, 1986.
12. Nakazawa, S.: The MHOST Finite Element Program: 3–D Inelastic Analysis Methods for Hot Section Components. User's Manual, NASA CR–182235, vols. 1 and 2, 1989.
13. Coker, D.; and Ashbaugh, N.E.: Characterization of Fracture in $[0/90]_{3s}$ SiC/1723 Composites. Report WL-TR–91–4119, March 1992.

REPORT DOCUMENTATION PAGE

Form Approved
OMB No. 0704-0188

Public reporting burden for this collection of information is estimated to average 1 hour per response, including the time for reviewing instructions, searching existing data sources, gathering and maintaining the data needed, and completing and reviewing the collection of information. Send comments regarding this burden estimate or any other aspect of this collection of information, including suggestions for reducing this burden, to Washington Headquarters Services, Directorate for Information Operations and Reports, 1215 Jefferson Davis Highway, Suite 1204, Arlington, VA 22202-4302, and to the Office of Management and Budget, Paperwork Reduction Project (0704-0188), Washington, DC 20503.

1. AGENCY USE ONLY (*Leave blank*)

2. REPORT DATE
April 1996

3. REPORT TYPE AND DATES COVERED
Technical Memorandum

4. TITLE AND SUBTITLE
The C(T) Specimen in Laminated Composites Testing

5. FUNDING NUMBERS
WU–50B–63–5B

6. AUTHOR(S)
Levon Minnetyan and Christos C. Chamis

7. PERFORMING ORGANIZATION NAME(S) AND ADDRESS(ES)
National Aeronautics and Space Administration
Lewis Research Center
Cleveland, Ohio 44135–3191

8. PERFORMING ORGANIZATION REPORT NUMBER
E–9840

9. SPONSORING/MONITORING AGENCY NAME(S) AND ADDRESS(ES)
National Aeronautics and Space Administration
Washington, DC 20546–0001

10. SPONSORING/MONITORING AGENCY REPORT NUMBER
NASA TM–4712

11. SUPPLEMENTARY NOTES
Portions of this material were presented as an invited paper at the Sixth Symposium on Composites, Fatigue, and Fracture sponsored by the American Society for Testing and Materials, Denver, Colorado, May 16–18, 1995. Levon Minnetyan, Clarkson University, Department of Civil and Environmental Engineering, Potsdam, New York 13699–5710; Christos C. Chamis, NASA Lewis Research Center. Responsible person, Christos C. Chamis, organization code 5200, (216) 433–3252.

12a. DISTRIBUTION/AVAILABILITY STATEMENT
Unclassified - Unlimited
Subject Category 24

This publication is available from the NASA Center for Aerospace Information, (301) 621–0390.

12b. DISTRIBUTION CODE

13. ABSTRACT ***(Maximum 200 words)***
The use of the compact tension C(T) specimen in laminated composites testing is investigated by considering two examples. A new computational methodology that scales up constituent material properties and stress and strain limits to the structure level is used to evaluate damage propagation stages as well as the structural fracture load. Damage initiation, growth, accumulation, progressive fracture, and ultimate fracture modes are identified. Specific dependences of C(T) specimen test characteristics on laminate configuration and composite constituent properties are quantified.

14. SUBJECT TERMS
Composites; Computational simulation; Damage; Degradation; Durability; Fracture; Laminates; Structural degradation

15. NUMBER OF PAGES
17

16. PRICE CODE
A03

17. SECURITY CLASSIFICATION OF REPORT
Unclassified

18. SECURITY CLASSIFICATION OF THIS PAGE
Unclassified

19. SECURITY CLASSIFICATION OF ABSTRACT
Unclassified

20. LIMITATION OF ABSTRACT